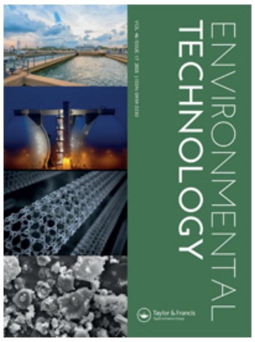

Taylor & Francis
Taylor & Francis Group

Environmental Technology

ISSN: 0959-3330 (Print) 1479-487X (Online) Journal homepage: www.tandfonline.com/journals/tent20

CO_2 emission dispersion of multiple point sources in the localized regions together with its intensity inversion model

Hanlin Xiao, Jiaheng Yang, Peng Gao, Jingjing Ai, Xiaochen Hu, Zhongyi Han & Tingting Fan

To cite this article: Hanlin Xiao, Jiaheng Yang, Peng Gao, Jingjing Ai, Xiaochen Hu, Zhongyi Han & Tingting Fan (2025) CO_2 emission dispersion of multiple point sources in the localized regions together with its intensity inversion model, Environmental Technology, 46:17, 3308-3319, DOI: 10.1080/09593330.2025.2463034

To link to this article: https://doi.org/10.1080/09593330.2025.2463034

ENVIRONMENTAL TECHNOLOGY
2025, VOL. 46, NO. 17, 3308–3319
https://doi.org/10.1080/09593330.2025.2463034

CO_2 emission dispersion of multiple point sources in the localized regions together with its intensity inversion model

Hanlin Xiao, Jiaheng Yang, Peng Gao, Jingjing Ai, Xiaochen Hu, Zhongyi Han and Tingting Fan

College of Mathematical and Physical Sciences, Shandong Advanced Optoelectronic Materials and Technologies Engineering Laboratory, Qingdao University of Science and Technology, Qingdao, People's Republic of China

ABSTRACT

The rapid and stable monitoring of CO_2 emissions from point sources in localized regions remains a key challenge in energy conservation and emission reduction efforts. To address this challenge, the Gaussian plume model is adopted for the rapid prediction of carbon emission dispersion from multiple point sources, and an inversion model for carbon emission intensities is constructed based on the Simplex search algorithm. By incorporating elevation data, the Gaussian plume model is modified to adapt to undulating mountainous terrain, and the impacts of the Gaussian diffusion model on the CO_2 concentration diffusion of multiple point sources are analyzed under the conditions of the observation height, atmospheric stability and terrain correction. When the number of monitoring stations reach 10, the average inversion error ranges from 0.01 to 0.47% under various atmospheric conditions, together with an average inversion uncertainty in a range of [0.09%, 1.22%], indicating that enhancing the number of monitoring stations and selecting more stable atmospheric conditions can significantly improve the inversion accuracy of the carbon emission intensities from multiple point sources. This work provides a theoretical guidance for formulating the energy conservation and emission reduction policies together with monitoring and reducing the anthropogenic carbon emission.

ARTICLE HISTORY
Received 9 July 2024
Accepted 15 January 2025

KEYWORDS
Carbon emission monitoring model; carbon emissions data inversion; Gaussian plume model; multiple point sources; Simplex search algorithm

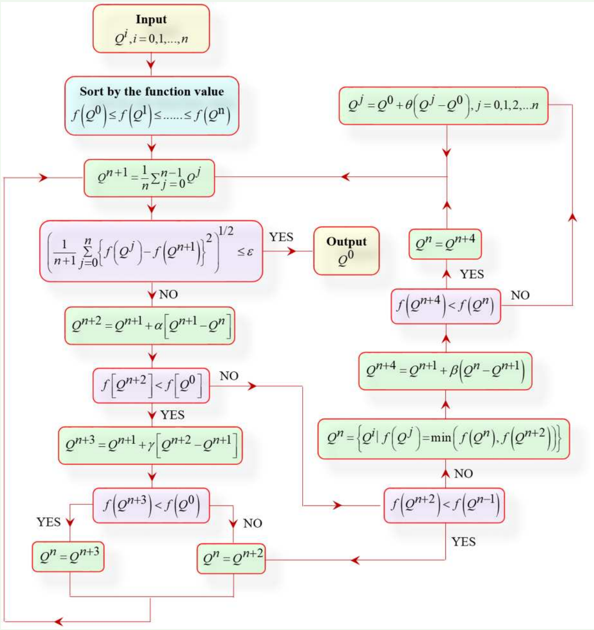

1. Introduction

Globally, the carbon dioxide (CO_2) emission has become one of the primary greenhouse gases posing a threat to the environment [1–6], and it accounts for about 80% emissions of the global greenhouse gases [7–9]. These emissions primarily come from human activities, such as the combustion of the fossil fuels for obtaining the energy and meeting the transportation need. Because

CONTACT Jingjing Ai jjaiqust@163.com College of Mathematical and Physical Sciences, Shandong Advanced Optoelectronic Materials and Technologies Engineering Laboratory, Qingdao University of Science and Technology, Qingdao 266061, People's Republic of China

of the growing demands of the humanity, the energy consumption exhibits an exponential increase. Currently, the fossil fuel combustion provides about 85% of the required energy, ultimately resulting in the increasing of the CO_2 concentration in the atmosphere [10]. In view of the global warming problem, approximately 200 countries reached a consensus on the Paris Agreement starting in 2015, and this agreement aims to reduce the CO_2 emission for keeping the global average temperature rise below 2°C [11–14]. It is a serious challenge for nations to achieve net-zero carbon emissions, which requires a timely, accurate monitoring and assessment for the anthropogenic carbon emissions.

An integral aspect of the carbon emission assessment involves simulating the CO_2 dispersion in the atmosphere based on identified emission sources. When simulating the gas dispersion from the point source, it is essential to choose an appropriate model based on the meteorological condition, terrain, gas characteristic and the nature of the emission source. As a semi-empirical model, the Gaussian plume model (GPM) can provide an analytical solution to the transport-dispersion equation for the air pollutants emitted in short or continuous periods [15–19]. As the GPM does not account for complex fluid dynamic effects, it is more suited to the localized flat terrain together with the uniform and stable wind conditions. It is assumed that the emission source is a continuous and steady release of gas, with its concentrations following a normal distribution in horizontal and vertical directions. Due to the simple expression, low computational cost and relatively reliable simulation result, the GPM is widely used in the simulation of atmospheric pollutants from the fixed point source, and the exact result under the complex terrain condition can be obtained with an appropriate adjustment. The multiple linear regression model and GPM is used for atmospheric dispersion research, achieving an accuracy of up to 84.2% for studying the spread of diseases in tomato plants [20]. The GPM is modified and validated to calculate the transmission of the ammonia and particulate matter from the ventilation tunnel fans in poultry houses [21]. The parameters affecting the gas diffusion are given by the gas diffusion mechanism and GPM in the process of natural gas leakage, and the Phast software is adopted to study the influences of various factors on the gas diffusion [22]. The Python programming language is utilized to model the Gaussian dispersion equation within the Quantum Geographic Information System, and the impacts of the pollutants emitted from the Kirkuk cement plant on the land cover are assessed [23]. The deterministic method based on the GPM is adopted to assess the dispersion of the PM2.5 pollutant of the air during fires [24].

In the carbon emission assessment, another critical requirement relates to the inversion of the carbon emission intensities (CEI) for the emission sources. Multiple temporally correlated sources are incorporated into a Bayesian framework, and the solution based on the GPM is employed to estimate the unorganized emission rates of the particulate matter from these sources [25]. An enhanced near-field Gaussian plume inversion method is adopted to quantify the emission from the point source along the downwind vertical plane [26]. The GPM in conjunction with the OCO-2/3 satellite data is applied to invert the CO_2 emissions from major power plants in China [27–28]. A novel Gaussian dispersion modeling method is introduced to estimate the methane emission from landfill sites, which collect the on-site methane concentration data by the mobile ground-based cavity ring-down spectrometer platform [29]. The Gaussian plume dispersion model along with a genetic algorithm is adopted to invert the location and the concentration of the sulfur dioxide emissions from a single ship [30]. The inversion method based on the probabilistic model demands a substantial volume of data together with the significant upfront effort, rendering its implementation challenging.

In view of the limitations of the existing research on the carbon emission diffusion tracking and monitoring inversion from multiple point sources in small areas, this study utilizes the GPM to simulate the spatial concentration distribution of CO_2 emissions from multi-point sources, and analyzes the influences of various factors on the CO_2 diffusion pattern. On basis of the GPM, an optimized inversion model is developed for the inversion of CEI from multi-point sources by integrating the Simplex search algorithm (SSA). Besides, a comparative analysis of various application scenarios such as different monitoring stations and atmospheric conditions is performed, and the uncertainty metrics is introduced to systematically assess the accuracy and stability of the model.

2. CO_2 emission diffusion from multiple point sources

2.1. Gaussian plume model

According to the GPM, the dispersion of the CO_2 emitted from the point source is simulated, and a coordinate system is established as shown in Figure 1. Where the emission source is located at the origin, together with the x and z axes pointing to the wind direction and

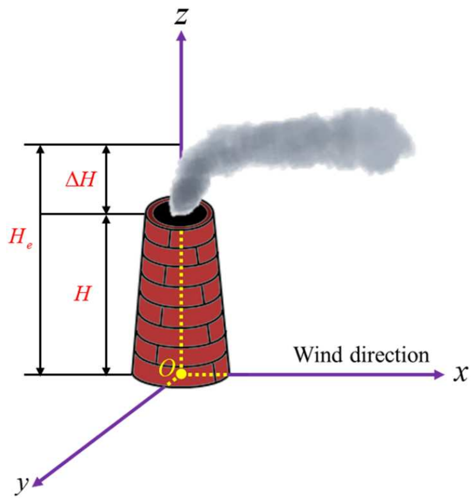

Figure 1. Schematic diagram of the carbon emissions from point sources.

vertical direction, respectively, and the y axis forms a right-hand spiral with the xz plane.

If considering the ground reflection and neglecting the ground absorption, the CO_2 concentration at arbitrary point can be expressed as:

$$C(x,y,z)=\frac{Q}{2\pi u\sigma_y\sigma_z}\exp\left(-\frac{y^2}{2\sigma_y^2}\right)\cdot\left\{\exp\left[-\frac{(z-H_e)^2}{2\sigma_z^2}\right]+\exp\left[-\frac{(z+H_e)^2}{2\sigma_z^2}\right]\right\},$$

where σ_y and σ_z represent the horizontal and vertical diffusion parameters respectively, which are determined by the downwind distance (x) and the atmospheric stability classes. For more details, refer to Appendix. Q and u stand for the CO_2 emission rate of the point source and the average wind speed at the chimney outlet, and H_e is the plume effective height calculated by equation (2).

$$\begin{aligned}H_e&=H+\Delta H\\&=H+\left[0.92V_sD+0.47\left(PV_s\frac{T_s-T_a}{T_s}\right)^{0.4}D^{0.8}H^{0.6}\right]/u,\end{aligned}$$

here H and ΔH refers to the chimney height and the plume rise height, respectively, while V_s and T_s are the flue gas emission velocity and temperature at the chimney outlet, together with the local atmospheric pressure, ambient temperature and the chimney outlet diameter being denoted by P, T_a and D. If considering multiple stable emission sources, it is necessary to establish a fixed coordinate system as shown in Figure 2.

The conversion relationship between the wind axis coordinate system (x, y, z) for single point source and the fixed coordinate system $(X, Y, Z)$for multiple point sources is written as:

$$\begin{cases}x=(X-X_0)\cos\theta+(Y-Y_0)\sin\theta\\y=(Y-Y_0)\cos\theta-(X-X_0)\sin\theta,\\z=Z\end{cases}$$

where the position of the point source is denoted as (X_0, Y_0) in the fixed coordinate system, while the angle of the wind axis coordinate system and fixed coordinate system is represented by θ. Thereby, the CO_2 concentration at arbitrary position for multiple point sources is changed as:

$$C(X,Y,Z)=\sum_{i=1}^{n}\frac{Q_i}{2\pi u\sigma_{y,i}\sigma_{z,i}}\exp\left(-\frac{y_i^2}{2\sigma_{y,i}^2}\right)\cdot\left\{\exp\left[-\frac{(z_i-H_{e,i})^2}{2\sigma_{z,i}^2}\right]+\exp\left[-\frac{(z_i+H_{e,i})^2}{2\sigma_{z,i}^2}\right]\right\}.$$

The Gaussian plume model is commonly employed to describe the diffusion of CO_2 under flat terrain conditions. In complex topographies, the model parameters must be adjusted according to atmospheric stability. Under neutral or unstable atmospheric conditions, the influence of atmospheric turbulence on the plume is significant, complicating plume analysis. Consequently, the impact of terrain on plume diffusion is often disregarded. In contrast, under stable atmospheric conditions, atmospheric turbulence is relatively weak. Even when neglecting the turbulence and fluid dynamics effects induced by the terrain, topographic variations still have a pronounced effect on the effective plume height, causing it to rise or fall significantly in response to changes in terrain. Therefore, based on the above considerations, the modified model adjusts the effective height to account for the influence of the

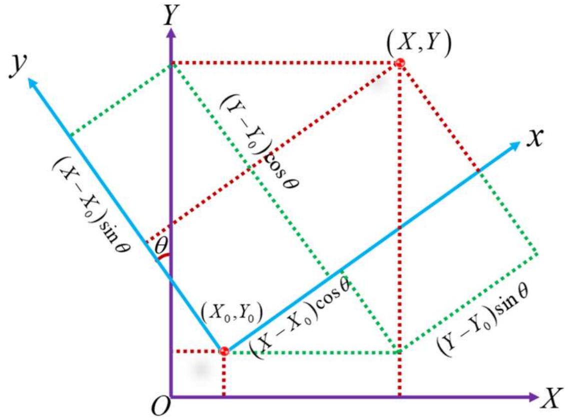

Figure 2. Transformation relationship between the wind axis coordinate and fixed coordinate system.

Table 1. Locations of the point sources together with the CO_2 emission data.

Emission source	Latitude	Longitude	Q (mg/s)	H (m)	D (m)	V_s (m/s)	T_s (K)
A	36.4	120.355	19,500,000	70	1.5	15	322
B	36.39	120.35	24,500,000	90	2	15	322
C	36.395	120.37	26,000,000	110	2.5	20	333
D	36.4	120.38	28,500,000	130	3	25	343
E	36.37	120.347	21,500,000	80	2	15	322
F	36.382	120.343	30,000,000	130	3	25	345

terrain, and it is expressed as follows:

$$C(x, y, z) = \frac{Q}{2\pi u \sigma_y \sigma_z} \exp\left(-\frac{y^2}{2\sigma_y^2}\right) \cdot \left\{\exp\left[-\frac{(z-(H_e-h_f))^2}{2\sigma_z^2}\right] + \exp\left[-\frac{(z+(H_e-h_f))^2}{2\sigma_z^2}\right]\right\},$$

where h_f represents the difference in the ground level between the point source (x, y, z) and the origin of coordinate.

2.2. Impact of various factors on the CO_2 emission diffusion

According to the relevant data of the Qingdao Shunan thermal power company, the locations of several emission sources together with the CO_2 emission data are drafted in Table 1. It is essential to emphasize that the emission information provided in this paper is intended exclusively as an illustrative example for simulation calculations.

2.2.1. CO_2 concentrations at different observation heights

In order to analyze the influences of different observation heights on the CO_2 diffusion, a simulated example is performed, and the spatial distributions of the CO_2 concentrations corresponding to various observation heights are displayed in Figure 3 with the topographic map as the background. Where the X-axis represents the eastward direction for all CO_2 concentration distribution maps while the Y-axis stands for the northward direction. Assuming that the environmental conditions characterized by the atmospheric stability level of D together with the surface wind speed of 2.5 m/s and the wind direction of an east-southeast 45° deviation, the plume effective heights for each emission source are calculated as 115, 167, 234 and 270 m above ground, respectively. On the basis of Figure 3, it is evident that the CO_2 plume primarily disperses along the wind axis, exhibiting a certain diffusion in both horizontal and vertical directions with a normal distribution pattern. For each emission source, the CO_2 concentration arrives at the maximum

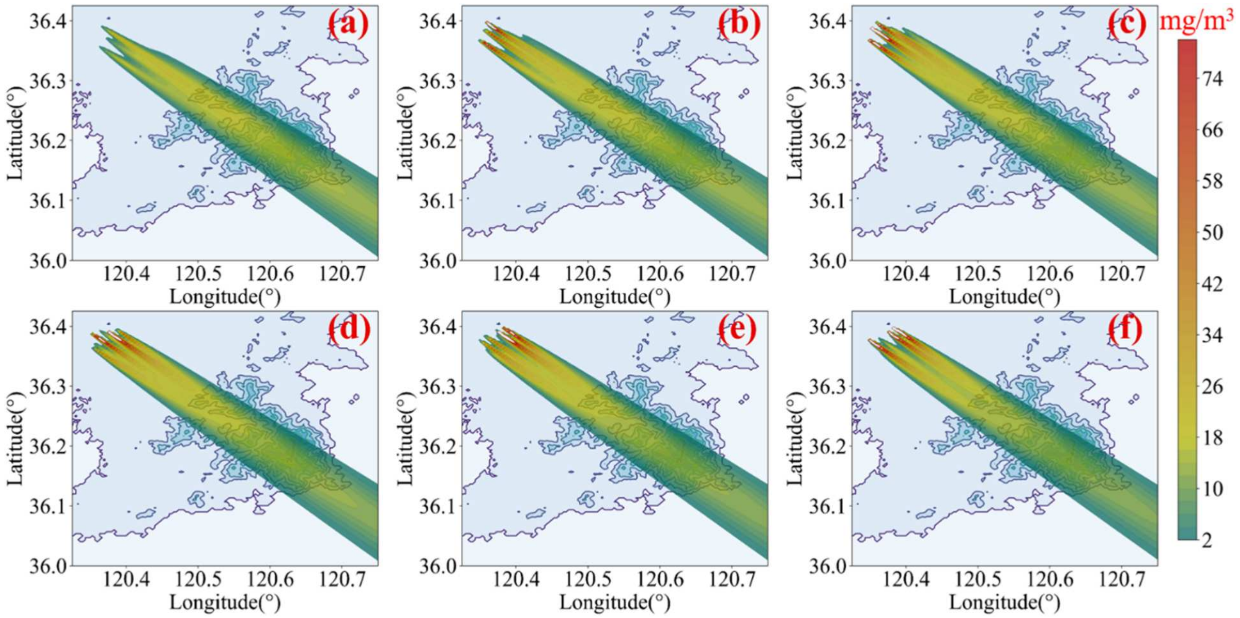

Figure 3. CO_2 concentration distributions at the observation heights of (a) 10 m, (b) 115 m, (c) 170 m, (d) 230 m, (e) 270 m and (f) 310 m above ground, respectively.

at the plume effective height along with the diffusion range being the widest. Importantly, near the ground level, the CO_2 concentration does not begin to accumulate significantly at the point source, but rather manifests itself at the ground reflection locations of each source. The A-type emission source has the most significant effect on the CO_2 concentration near the ground level, indicating that small emission sources lead to more CO_2 accumulation on the ground due to the lower chimney height.

2.2.2. Impacts of different atmospheric stabilities on the CO_2 diffusion

For the constant wind speed, different observation times and cloud cover will cause different atmospheric states, thus affecting the atmosphere vertical movement. For different atmospheric stabilities, the CO_2 concentration distributions at the observation heights of 10, 170 and 310 m above ground are shown in Figures 4–6, where the atmospheric stability grades are denoted by the capital letters A, B, C, D, E and F from the most unstable to the most stable. By Figures 4–6, the atmospheric stability has an important impact on the CO_2 diffusion and transport. At the ground level, the unstable atmosphere is conducive to the CO_2 dissipating quickly, while the stable atmosphere causes the CO_2 to travel longer distances. Likewise, there are similar behaviors appearing around the effective height of 170 m and at higher altitude ($\geq$ 310m), but the influence of the atmospheric stability on the CO_2 concentration is minimal at the effective height of 170 m. The unstable atmosphere is commonly encountered during the daytime, and the vertical motion of the atmosphere is accelerated due to the ground being heated. The rising air carries the CO_2 to higher altitudes, which makes it rapidly diluted and dispersed, thereby reducing the CO_2 concentration at the ground level. The stable atmosphere usually appears at night or early in the morning, and the cold air descents at this time, thus forming a stable atmosphere layer. It limits the CO_2 diffusion and results in a longer transport distance.

2.2.3. Impact of the terrain height on the CO_2 diffusion

Based on the terrain correction method described in equation (5) of Section 2.1, Figures 7 and 8 depict the distribution of CO_2 concentrations at different observational altitudes above ground before and after the correction. For regions with an atmospheric stability class of E. Post-correction, the CO_2 concentration displays a strange distribution, with the terrain's influence on concentration patterns being most pronounced in mountainous areas. The reason is that the elevated terrain shortens the distance between the ground and the plume centerline, and the CO_2 concentration increases with the observation location getting closer to the plume centerline. However, as the observational altitude exceeds the plume centerline and rises to greater heights, the CO_2 concentration gradually decreases.

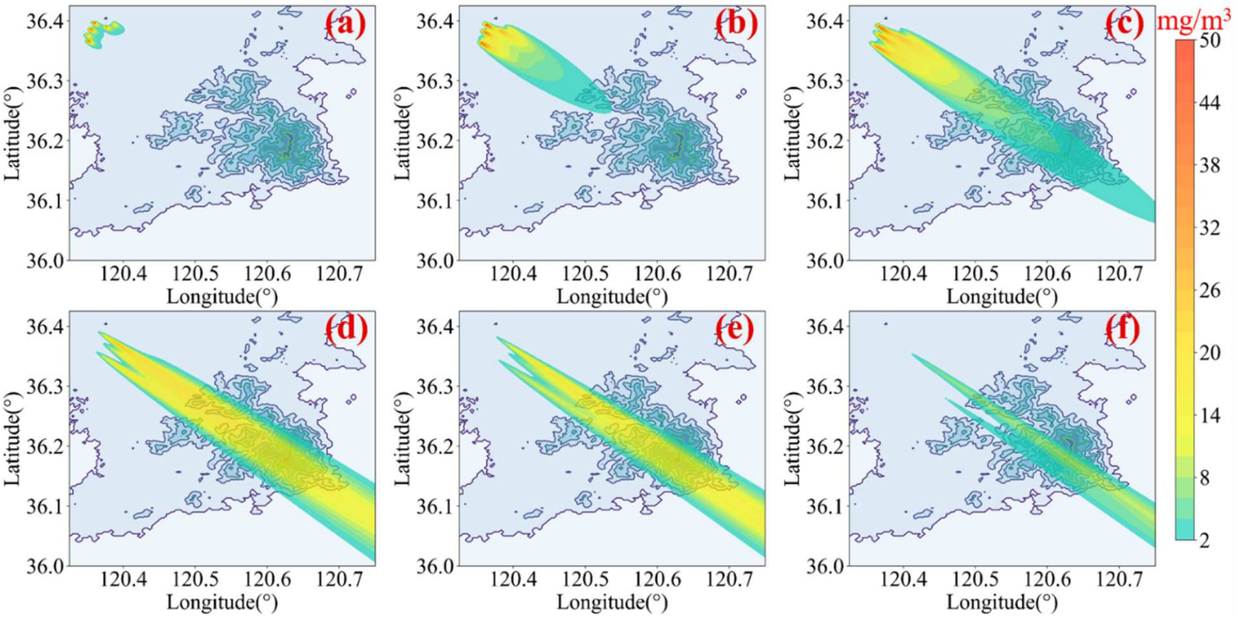

Figure 4. CO_2 concentration distributions at the observation height of 10 m above ground corresponding to the atmospheric stability grades of (a) A, (b) B, (c) C, (d) D, (e) E and (f) F, respectively.

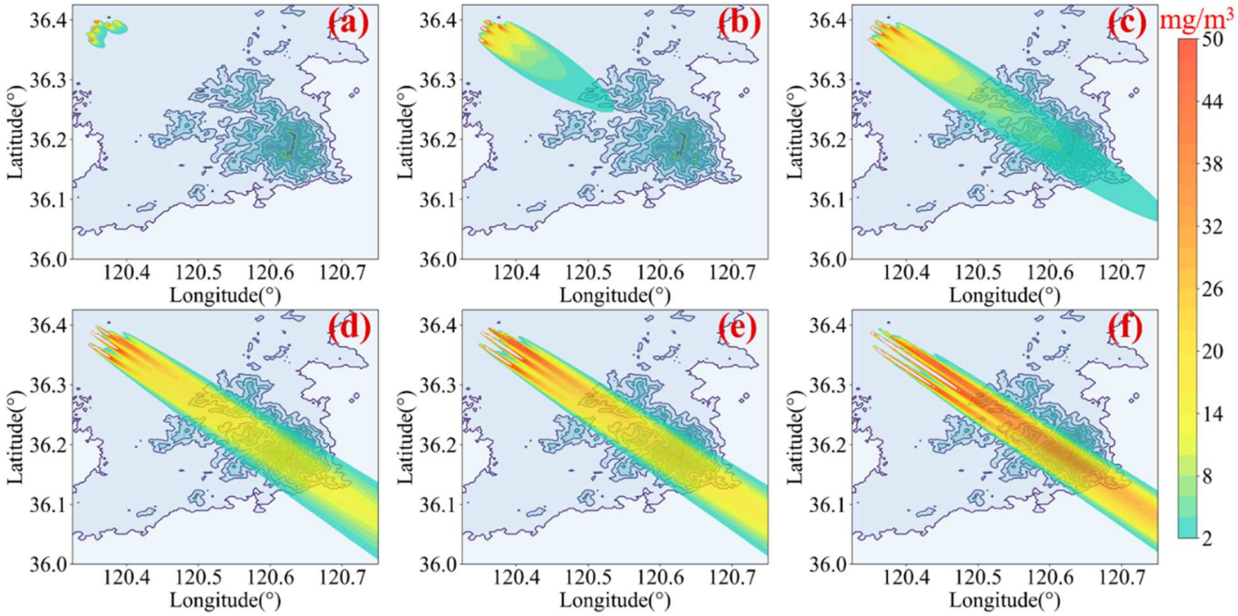

Figure 5. CO_2 concentration distributions at the observation height of 170 m above ground corresponding to the atmospheric stability grades of (a) A, (b) B, (c) C, (d) D, (e) E and (f) F, respectively.

3. Carbon emission data inversion from multiple point source

3.1. Inversion algorithm

The Simplex search algorithm (SSA), as an optimization inversion method, accurately estimates the CEI of a source by minimizing the error between the model's simulated results and the observational data. Through iterative optimization of initial values, the algorithm continues until the objective function converges as shown in equation (6), thereby transforming the inversion problem of point-source CEI into a problem of finding the minimum value.

$$f(Q^i) = \sum (C_{\text{measure}} - C^i_{\text{calc}})^2,$$

where Q^i represents the CEI after iterative optimization, and C_{measure} denotes the measured CO_2 concentration at a specific height of the downwind monitoring station

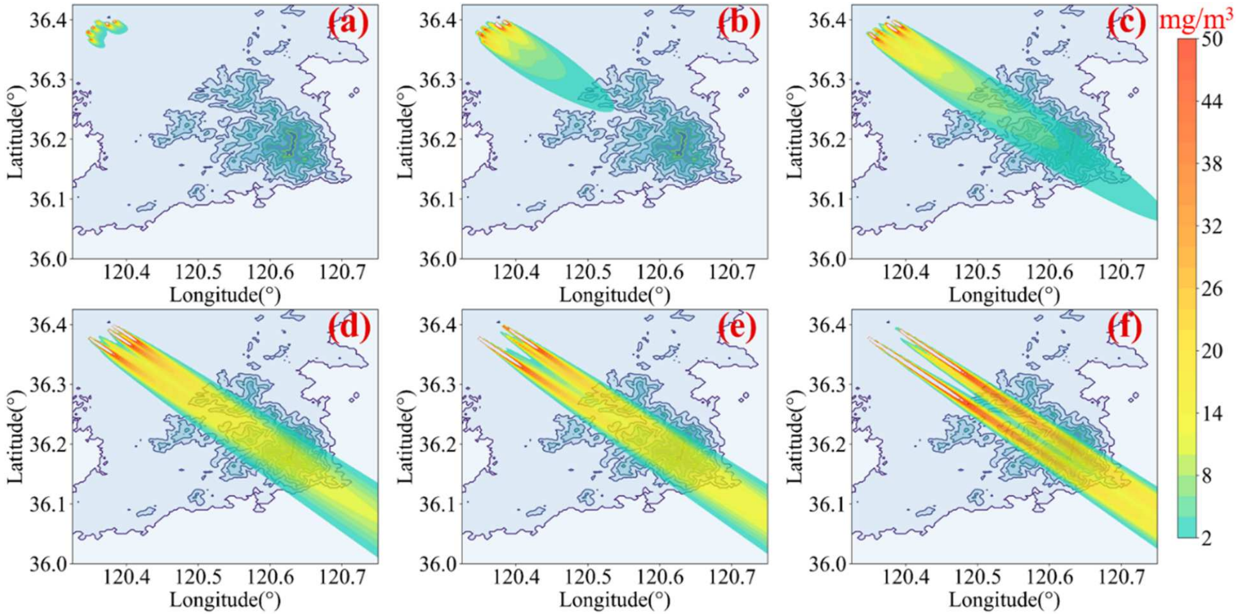

Figure 6. CO_2 concentration distributions at the observation height of 310 m above ground corresponding to the atmospheric stability grades of (a) A, (b) B, (c) C, (d) D, (e) E and (f) F, respectively.

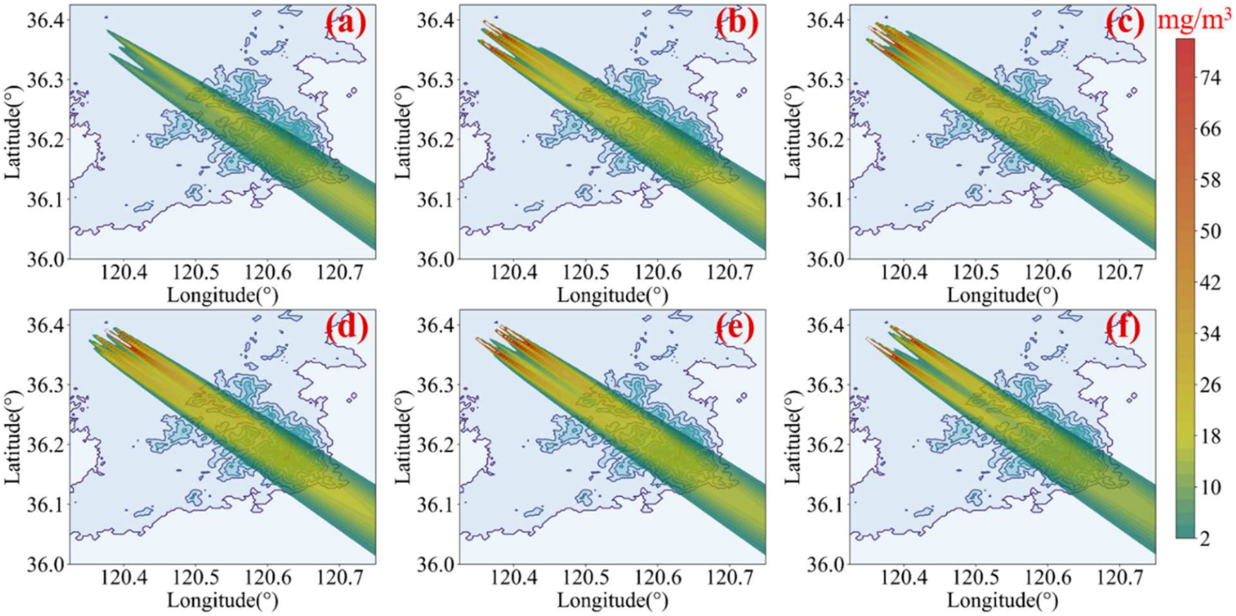

Figure 7. CO_2 concentration distributions at the observation heights of (a) 10 m, (b) 115 m, (c) 170 m, (d) 230 m, (e) 270 m and (f) 310 m above ground if the terrain correction not being considered.

while C^i_{calc} refers to the simulated CO_2 concentration at the same height of the same station, as predicted by the GPM with Q^i as the input. The flow of an independent inversion experiment using SSA is shown in Figure 9, which mainly includes key modules such as sorting, optimization, judgment, input and output.

The model first randomly selects $n + 1$ sets of initial Q and inputs them into the algorithm, where n is the number of downwind monitoring sites. Subsequently, these initial Q are arranged in ascending order based on the value of the objective function f. Next, the new Q is generated using coefficients related to reflection (α), shrinkage (β), expansion (γ) and compression (θ) within the model. The selection process, guided by a decision-making module, progressively filters out the Q that further minimize the objective function f until the predefined precision criteria (ε) are met. Ultimately, the algorithm outputs the optimal solution.

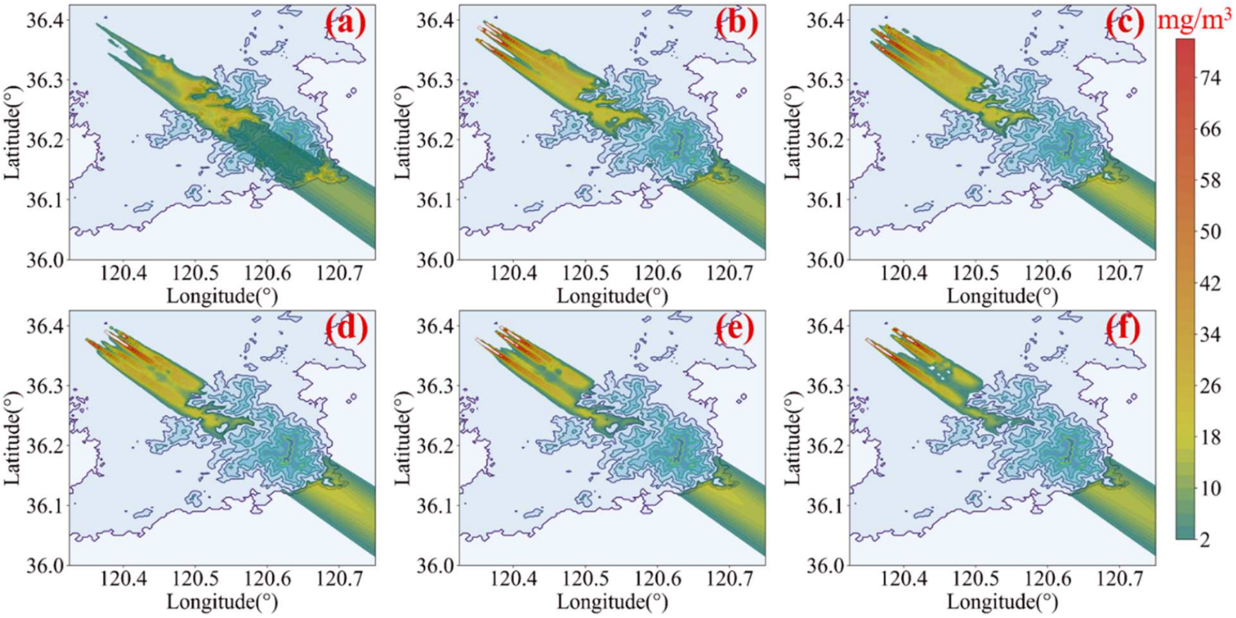

Figure 8. CO_2 concentration distributions at the observation heights of (a) 10 m, (b) 115 m, (c) 170 m, (d) 230 m, (e) 270 m and (f) 310 m above ground if the terrain correction being considered.

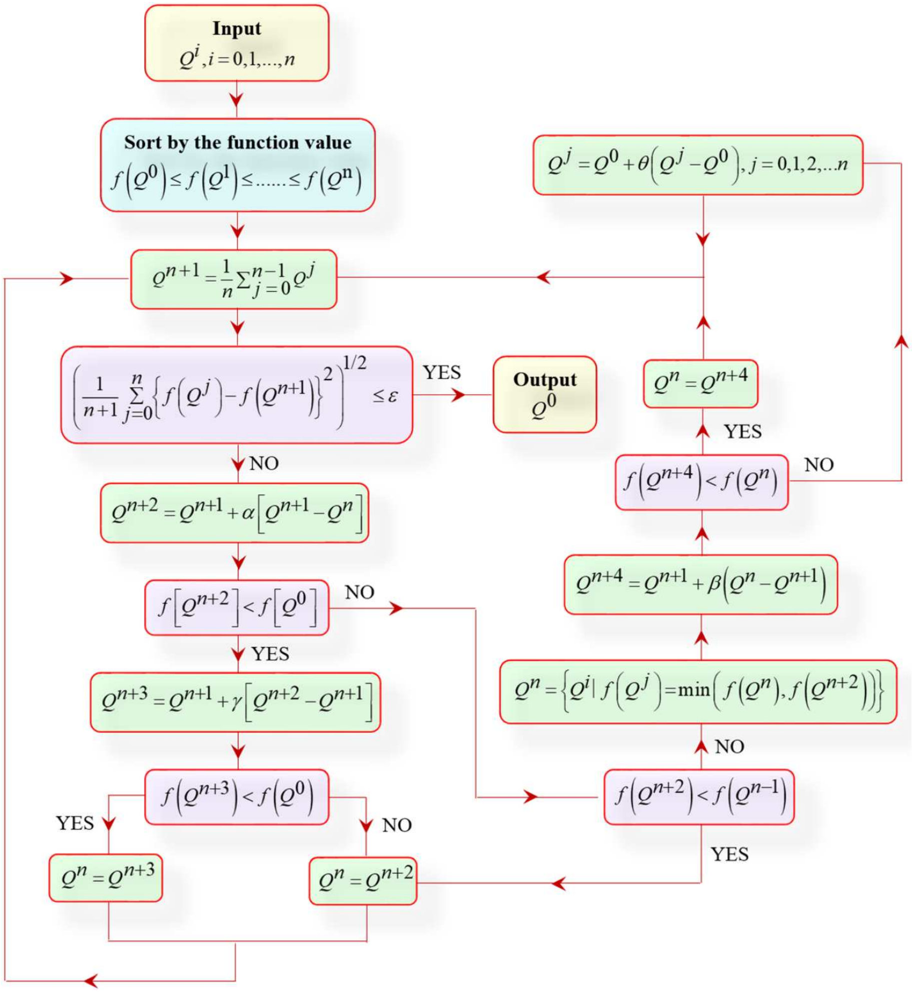

Figure 9. Flow chart of the inversion algorithm.

3.2. Inversion experiment

Before conducting the inversion experiments, it is a crucial step to acquire CO_2 concentration data from monitoring stations. However, the CO_2 concentration datasets provided by these monitoring stations are often not publicly available. Therefore, the CO_2 concentration data at the monitoring station locations is simulated based on the actual carbon emission data of emission sources presented in Table 1 together with the GPM outlined in Section 2. These simulated concentrations serve as the monitoring values required for the inversion model. To ensure that the concentrations at the monitoring sites are representative and relevant, in each independent inversion experiment, ten monitoring stations are randomly selected in regions downwind of the emission sources where the CO_2 concentration exceeds $15 mg/m^3$. An example of a randomly selected set of monitoring sites is shown in Figure 10. The monitoring heights of each station range from 10 to 100 m above the ground, allowing for a comprehensive representation of the CO_2 concentration distribution at different vertical levels.

For the six point sources listed in Table 1, 11 sets of initial estimates for the CEI were randomly selected

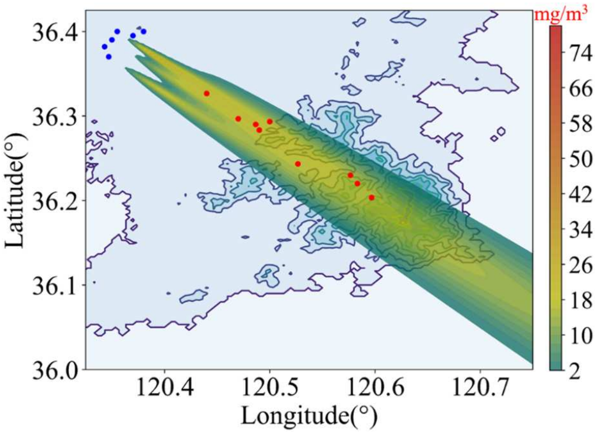

Figure 10. Location map of the downwind monitoring stations.

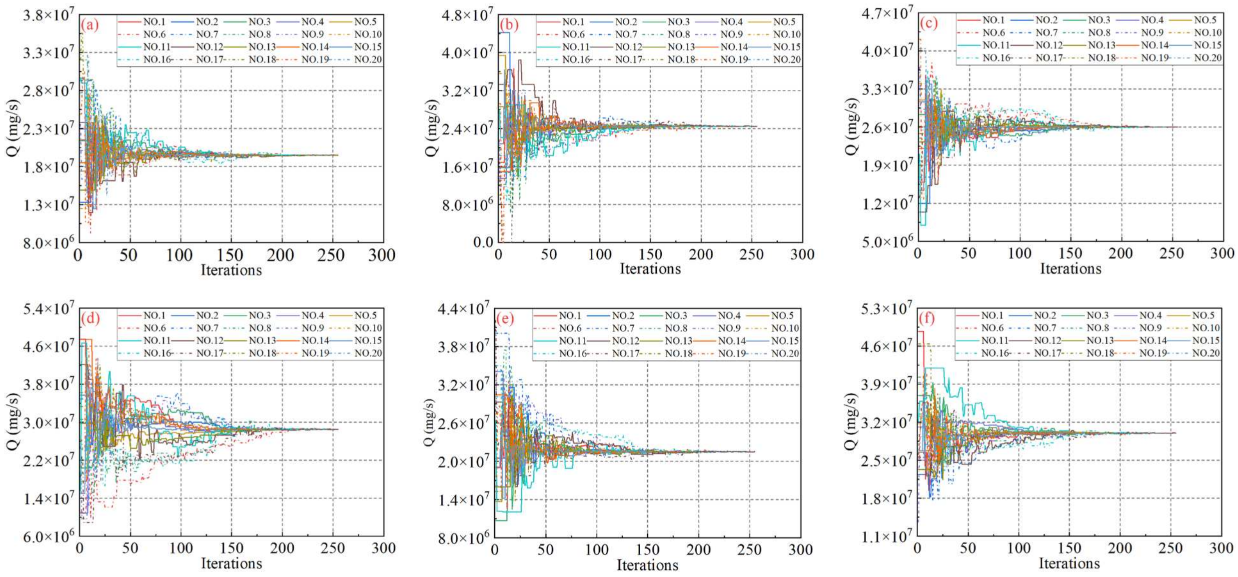

Figure 11. Inversion processes of the CEI for point sources (a) A, (b) B, (c) C, (d) D, (e) E, and (f) F.

within the range of [0, 5×10^7]mg/s. The parameters in the optimization model were set as follows: $\alpha = 1$, $\gamma = 2$, $\beta = 0.5$, $\theta = 0.9$, and the precision requirement was set to $\varepsilon = 0.001$. Figure 11 illustrates the variation in the CEI of six point sources across 20 independent inversion experiments under atmospheric conditions with a stability class of E and a wind speed of 2 m/s. Due to the random selection of initial estimates, the number of iterations differs for each inversion experiment, and the convergence rates also vary for different point sources. The 12th and 17th inversion experiments required the most iterations, both reaching the precision requirement after 255 iterations and successfully yielding the optimal solution.

For the point source A, the initial estimate of CEI ranges from 1.25×10^7 to 2.343×10^7mg/s, exhibiting a relatively fast convergence rate, with the inversion results stabilizing after 150 iterations. For point sources B, C, and E, the distributions of initial estimates are quite similar, primarily concentrated between 1.0×10^7 and 4.4×10^7mg/s, with the point source B exhibiting the widest range of initial estimates. During the first 150 iterations, the point source B converges quickly, while the convergence of point sources C and E is relatively gradual. The initial estimates for point sources D and F are distributed within the ranges of $[1.09, 4.75] \times 10^7$ and $[1.36, 4.87] \times 10^7$ mg/s, respectively. Despite having similar initial ranges, the point source D demonstrates a noticeably slower convergence rate compared to the point source F.

The number of monitoring stations has a significant impact on the accuracy of the inversion model. Figure 12 presents the inversion results for the CEI of each point source across 20 inversion experiments,

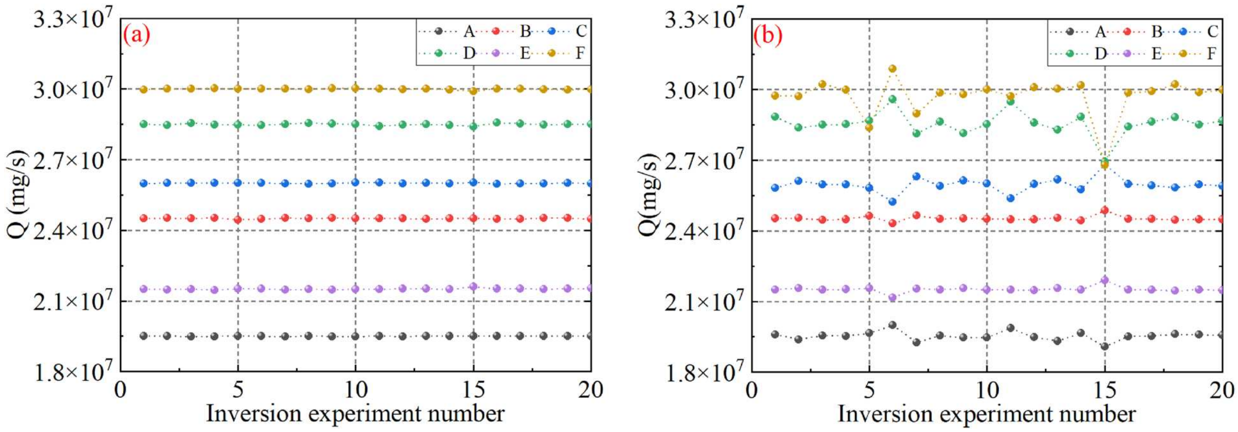

Figure 12. Inversion results of the CEI when the number of monitoring stations is (a) 10 and (b) 6.

with monitoring stations set to 10 and 6, respectively. The inversion error (IE) and uncertainty (Unc) are introduced to characterize the inversion accuracy and stability of the model, as shown in equation (7).

$$\begin{cases} IE = |\bar{Q} - Q_{act}|/Q_{act} \\ Unc = \sqrt{\frac{1}{m}\sum_{i=1}^{m}(Q_i - \bar{Q})^2}/\bar{Q} \end{cases}.$$

Here, m and Q_i represent the number of inversion experiments and the optimal solution for the CEI in each inversion experiment, respectively, while Q_{act} and $\bar{Q}$ stand for the actual values of the CEI and the average values of the results from m inversion experiments.

A comparison reveals that as the number of monitoring stations decreases, the inversion results for the CEI of the point sources exhibit varying degrees of fluctuation, with the point sources D and F showing the greatest fluctuation. When the number of monitoring stations is 10, the average inversion error and uncertainty for these point sources are 0.01 and 0.09%, respectively. As the number of monitoring stations decreases to 6, the inversion error and uncertainty increase significantly, reaching 0.27 and 1.32%, respectively. This is due to the reduced number of monitoring stations, which makes it difficult to ensure their uniform distribution in the downwind regions of the point sources. As a result, for the point sources D and F, the CO_2 concentrations obtained from the monitoring stations no longer adequately represent the overall emission characteristics.

Similarly, for the application of the inversion model under different atmospheric conditions, Table 2 compares the inversion results of the CEI for each point source when the number of monitoring stations is 10, excluding atmospheric stability classes of A and F. As shown in Table 2, the inversion accuracy of the model exhibits a downward trend as the atmospheric stability and wind speed decrease under different meteorological conditions. Notably, the impact of atmospheric stability on inversion accuracy is particularly significant. When the atmospheric stability is low, the diffusion ranges of CO_2 emitted by each point source decreases, and the CO_2 concentrations obtained by the monitoring stations may no longer reflect the combined effects of all point sources. In this case, the data quality from the monitoring stations deteriorates, weakening the inversion model's ability to distinguish the CEI of different point sources, thereby increasing the inversion error and uncertainty.

4. Conclusion

In this paper, the CO_2 diffusion from multiple point sources is studied in detail based on the Gaussian plume model, and the influences of different altitudes and atmospheric stabilities on the CO_2 diffusion are systematically analyzed. The terrain correction of the CO_2 diffusion under complex terrain conditions is carried out to obtain successfully the corrected diffusion data. In addition, this study develops an inversion model for the carbon emission intensities from multiple point sources based on the Simplex search algorithm, and compare the inversion results under different monitoring station densities and atmospheric conditions. The results demonstrate that increasing the number of monitoring stations and selecting more stable atmospheric conditions can significantly improve the inversion accuracy of the model. Under various atmospheric

Table 2. Inversion results of the CEI for each point source under different atmospheric conditions.

		Inversion result			
Emission source		$PS{:}E\ u = 2.0m/s$	$PS{:}D\ u = 1.5m/s$	$PS{:}C\ u = 2.0m/s$	$PS{:}B\ u = 1.5m/s$
A	$\bar{Q}(mg/s)$	19,501,800	19,503,500	19,473,900	19,550,300
	$IE(\%)$	0.01	0.018	0.134	0.258
	$Unc(\%)$	0.047	0.115	0.765	0.617
B	$\bar{Q}(mg/s)$	24,499,400	24,498,700	24,515,600	24,589,300
	$IE(\%)$	0.002	0.005	0.064	0.364
	$Unc(\%)$	0.089	0.1	0.297	1.029
C	$\bar{Q}(mg/s)$	25,999,500	26,003,500	26,026,200	25,760,200
	$IE(\%)$	0.002	0.013	0.101	0.922
	$Unc(\%)$	0.061	0.194	0.715	2.029
D	$\bar{Q}(mg/s)$	28,496,400	28,483,760	28,491,900	28,751,800
	$IE(\%)$	0.013	0.057	0.028	0.884
	$Unc(\%)$	0.144	0.27	0.427	2.153
E	$\bar{Q}(mg/s)$	21,502,500	21,507,000	21,539,100	21,448,500
	$IE(\%)$	0.012	0.033	0.182	0.24
	$Unc(\%)$	0.095	0.128	0.821	0.825
F	$\bar{Q}(mg/s)$	29,996,700	30,014,800	29,947,200	29,949,100
	$IE(\%)$	0.011	0.049	0.176	0.17
	$Unc(\%)$	0.089	0.248	0.671	0.654

conditions, the average inversion error of the model ranges from 0.01 to 0.47%, while the average inversion uncertainty changing from 0.09 to 1.22%. These results validate the effectiveness of the Gaussian plume model and the Simplex search algorithm in monitoring CO_2 emissions from multi-point sources in localized regions.

Acknowledgment

I would like to thank Jiaheng Yang, Peng Gao and Tingting Fan for providing me with theoretical guidance, together with Jingjing Ai for providing language help, writing help and proofreading the paper.

Disclosure statement

No potential conflict of interest was reported by the author(s).

Funding

This research was supported by the Natural Science Foundation of Shandong Province (ZR2024MF098, ZR2022MF266).

References

[1] Garg AP, Chaudhary M, Garg C. impact of carbon emissions and strategies for its management. In: Chapter 4: Quality of life and climate change: impacts, sustainable adaptation, and social-ecological resilience. USA: Pennsylvania; 2024. p. 75–107.

[2] Zhang S, Shen Y, Wang L, et al. Phase change solvents for post-combustion CO_2 capture: principle, advances, and challenges. Appl Energy. 2019;239:876–897. doi:10.1016/j.apenergy.2019.01.242

[3] Yasser N, Samer A. Economical and environmental feasibility of the renewable energy as a sustainable solution for the electricity crisis in the Gaza Strip. Int J Eng Res Dev. 2016;12(3):35–44.

[4] Fathi NY, Ali AK., Abdulsalam IM, et al. Economical and environmental assessment of electrical generators: A case study of Southern Region of Libya. Int J Energy Policy Manag. 2016;1(4):64–71.

[5] Hafez AA, Fathi NY, Hammdan MI, et al. Technical and economic feasibility of utility-scale solar energy conversion systems in Saudi Arabia. Iran J Sci Technol Trans Electr Eng. 2020;44:213–225. doi:10.1007/s40998-019-00233-3

[6] Yoro KO, Daramola MO. 2020. CO2 emission sources, greenhouse gases, and the global warming effect. In: Advances in carbon capture, Cambridge, UK; 2020. p. 3–28.

[7] Rezakazemi M, Darabi M, Soroush E, et al. Co2 absorption enhancement by water-based nanofluids of CNT and SiO2 using hollow-fiber membrane contactor. Sep Purif Technol. 2019;210:920–926. doi:10.1016/j.seppur.2018.09.005

[8] Ochedi FO, Yu J, Yu H, et al. Carbon dioxide capture using liquid absorption methods: a review. Environ Chem Lett. 2021;19:77–109. doi:10.1007/s10311-020-01093-8

[9] Omotoso AB, Omotayo AO. The interplay between agriculture, greenhouse gases, and climate change in Sub-Saharan Africa. Reg Environ Change. 2024;24:1. doi:10.1007/s10113-023-02159-3

[10] Younas M, Rezakazemi M, Daud M, et al. Recent progress and remaining challenges in post-combustion CO_2 capture using metal-organic frameworks (MOFs). Prog Energy Combust Sci. 2020;80:100849. doi:10.1016/j.pecs.2020.100849

[11] Falkner R. The Paris agreement and the new logic of international climate politics. Int Aff. 2016;92(5):1107–1125. doi:10.1111/1468-2346.12708

[12] Tanaka K, Neill BCO. The Paris agreement zero-emissions goal is not always consistent with the 1.5 C and 2 C temperature targets. Nat Clim Change. 2018;8(4):319–324. doi:10.1038/s41558-018-0097-x

[13] Lee HS, Yap LT, Lee SY, et al. The impacts of ICT and innovation on carbon dioxide emissions in G20 countries. In: IOP Conference Series: Earth and Environmental Science, Kuala Lumpur, Malaysia; 2024. p. 1303(1): 012011.

[14] Adun H, Ampah JD, Bamisile O, et al. The synergistic role of carbon dioxide removal and emission reductions in achieving the Paris agreement goal. Sustain Prod Consum. 2024;45:386–407. doi:10.1016/j.spc.2024.01.004

[15] Snoun H, Krichen M, Chérif H. A comprehensive review of Gaussian atmospheric dispersion models: current usage and future perspectives. Euro-Mediterr J Environ Integr. 2023;8(1):219–242. doi:10.1007/s41207-023-00354-6

[16] Green AES, Singhal RP, Venkateswar R. Analytic extensions of the Gaussian plume model. J Air Pollut Control Assoc. 1980;30(7):773–776. doi:10.1080/00022470.1980.10465108

[17] Weil JC, Brower RP. An updated Gaussian plume model for tall stacks. J Air Pollut Control Assoc. 1984;34(8):818–827. doi:10.1080/00022470.1984.10465816

[18] Essa KSM, Taha HMA. Study Gaussian plume model and the gradient transport (K) of the advection-diffusion equation and its applications. MAUSAM. 2023;74(3):663–672. doi:10.54302/mausam.v74i3.5888

[19] Essa K, Elsaied S, Khalifa A, et al. A comparison between Gaussian plume models and analytical advection-diffusion equation in unstable condition. MAUSAM. 2023;74(1):11–18. doi:10.54302/mausam.v74i1.4550

[20] Miriyagalla R, Samarawickrama Y, Rathnaweera D, et al. 2019. On the effectiveness of using machine learning and Gaussian plume model for plant disease dispersion prediction and simulation. In: International Conference on Advancements in Computing (ICAC), Trichy, India; 2019. p. 317–322.

[21] Yang Z, Yao Q, Buser MD, et al. Modification and validation of the Gaussian plume model (GPM) to predict ammonia and particulate matter dispersion. Atmos Pollut Res. 2020;11(7):1063–1072. doi:10.1016/j.apr.2020.03.012

[22] Wang B, Chen L, Lin W, et al. Research on gas diffusion of natural gas leakage based on Gaussian plume model. Arab J Geosci. 2022;15(7):619. doi:10.1007/s12517-022-09922-6

[23] Ajaj QM, Shafri HZM, Wayayok A, et al. Assessing the impact of Kirkuk Cement Plant Emissions on Land cover by Modelling Gaussian Plume with Python and QGIS.

Egypt J Remote Sens Space Sci. 2023;26(1):1–16. doi:10.1016/j.ejrs.2022.12.001

[24] Lotrecchiano N, Sofia D, Giuliano A, et al. Pollution dispersion from a fire using a Gaussian plume model. Int J Saf Secur Eng. 2020;10:431–439. doi:10.18280/ijsse.100401

[25] Hosseini B, Stockie JM. Bayesian estimation of airborne fugitive emissions using a Gaussian plume model. Atmos Environ. 2016;141:122–138. doi:10.1016/j.atmosenv.2016.06.046

[26] Hollenbeck D, Zulevic D, Chen Y. A modified near-field Gaussian plume inversion method using multi-sUAS for emission quantification. In: International Conference on Unmanned Aircraft Systems (ICUAS), Montreal, Canada; 2022. p. 1620–1625.

[27] Guo W, Shi Y, Liu Y, et al. Co_2 emissions retrieval from coal-fired power plants based on OCO-2/3 satellite observations and a Gaussian plume model. J Cleaner Prod. 2023;397:136525. doi:10.1016/j.jclepro.2023.136525

[28] Manheim DC, Newman S, Yeşiller N, et al. Application of cavity ring-down spectroscopy and a novel near surface Gaussian plume estimation approach to inverse model landfill methane emissions. MethodsX. 2023;10:102048. doi:10.1016/j.mex.2023.102048

[29] Peng X, Xiao C, Zheng F, et al. Estimation of single ship emission location and intensity inversion in port water. In: 5th International Conference on Transportation Information and Safety (ICTIS), Changsha, People's Republic of China; 2019. p. 236–241.

[30] Li Y, Jiang F, Jia M, et al. Improved estimation of CO2 emissions from thermal power plants based on OCO-2 XCO2 retrieval using inline plume simulation. Sci Total Environ. 2024;913:169586. doi:10.1016/j.scitotenv.2023.169586

Appendix. Determination of the horizontal and vertical diffusion parameters (σ_y,σ_z)

Table A1. Horizontal diffusion parameter.

Horizontal diffusion parameter	Atmospheric stability classes	γ_1	α_1	Downwind distance (m)
$\sigma_y = \gamma_1 X^{\alpha_1}$	A	0.425809	0.901074	0~1000
		0.602052	0.850934	>1000
	B	0.281846	0.914370	0~1000
		0.396353	0.865014	>1000
	BC	0.229500	0.919325	0~1000
		0.314238	0.875086	>1000
	C	0.177154	0.924279	0~1000
		0.232123	0.885157	>1000
	CD	0.143940	0.926849	0~1000
		0.189396	0.886940	>1000
	D	0.110726	0.929418	0~1000
		0.146669	0.888723	>1000
	DE	0.098563	0.925118	0~1000
		0.124308	0.892794	>1000
	E	0.086400	0.920818	0~1000
		0.101947	0.896864	>1000
	F	0.055363	0.929418	0~1000
		0.073334	0.888723	>1000

Table A2. Vertical diffusion parameter.

Vertical diffusion parameter	Atmospheric stability classes	γ_2	α_2	Downwind distance (m)
$\sigma_z = \gamma_2 X^{\alpha_2}$	A	0.0799904	1.12154	0~300
		0.00854771	1.52360	300~500
		0.00021154	2.10881	>500
	B	0.127190	0.964435	0~500
		0.0570251	1.09356	>500
	BC	0.114682	0.941015	0~500
		0.0757182	1.00770	>500
	C	0.106803	0.917595	>0
	CD	0.126152	0.838628	0~2000
		0.235667	0.756410	2000~10,000
		0.136659	0.815575	>10,000
	D	0.104634	0.826212	1~1000
		0.400167	0.632023	1000~10,000
		0.810763	0.555360	>10,000
	DE	0.111771	0.776864	0~2000
		0.528992	0.572347	2000~10,000
		1.03810	0.499149	>10,000
	E	0.0927529	0.788370	0~1000
		0.433384	0.565188	1000~10,000
		1.73241	0.414743	>10,000
	F	0.060765	0.784400	0~1000
		0.370015	0.52596	1000~10,000
		2.40691	0.322659	>10,000

Reference

Technical methods for making local emission standards of air pollutants, GB/T 3840-91, 1992-06-01.